Chapter 24

Clayey Landslide Investigations using Active and Passive V_S Measurements

F. Renalier[1], G. Bièvre[1, 2], D. Jongmans[1], M. Campillo[1], and P.-Y. Bard[1]

Abstract

Clay slopes frequently are affected by gravitational movements. Such movements generate complex patterns of deformation that have slip surfaces located at different depths and are likely to modify geophysical parameters of the ground. Geophysical experiments performed on the large clayey Avignonet landslide (Western Alps, France) have shown that shear-wave velocity (V_S) is most sensitive to clay deconsolidation resulting from the slide. Values of V_S at shallow depths exhibit an inverse correlation with the GPS-measured surface-displacement rates. Compared with measurements in stable zones, V_S values in the most deformed areas of the slide can be reduced by a factor of two to three. Laboratory measurements on clay samples set in triaxial cells have shown that a strong decrease of V_S values accompanies an increase in the void ratio, in a velocity range similar to that measured in situ. Although other factors (stress change, cementation, granularity) can modify V_S values, these results justify the potential of V_S imaging to map spatially the deformation induced by a landslide. Several active and passive techniques for measuring V_S are tested and compared on the kilometer-size and 50-m-deep Avignonet landslide. The crosscorrelation technique, applied to seismic noise recorded by a large-aperture array and associated with shot records, turns out to be an effective tool for imaging the landslide in three dimensions. If permanent stations are installed, the same method also can be used to monitor the evolution of seismic velocity with time, as an indicator of landslide activity.

Introduction

Shear-wave velocity (V_S) has emerged increasingly as a key geophysical parameter for characterizing soil layers in geotechnical engineering. Compared with compressional waves, shear waves offer the advantages of a shorter wavelength and its resulting better resolution and of little sensitivity to the fluid saturation (Dasios et al., 1999). Whereas P-wave velocity (V_P) contrasts are small in saturated soils (Mondol et al., 2007), shear waves exhibit a wide range of velocity values, thereby allowing better detection of changes in lithology and compactness at shallow depths. Numerous studies (e.g., Hegazy and Mayne, 1995; Andrus et al., 2004; Hasancebi and Ulusay, 2007) have suggested relationships between V_S and the penetration resistance measured from the cone penetration test (CPT) and the standard penetration test (SPT), making V_S a meaningful geotechnical parameter. As a result, V_S has been used increasingly in a wide variety of applications, including delineation of geologic boundaries in the subsurface (e.g., Hunter et al., 2002; Ghose and Goudswaard, 2004), evaluation of ground densification (Kim and Park, 1999) and of landslide-related deconsolidation (Jongmans et al., 2009), and assessment of liquefaction potential (Finn, 2000). During earthquakes, ground motions may be amplified strongly at sites with soft layers that overlie bedrock. The main parameter controlling the dynamic-site response is shown to be the contrast in V_S values (e.g., Bard and Riepl-Thomas, 1999; Sommerville and Graves, 2003), and V_S in shallow layers is now considered to be the key

[1]*Laboratoire de Géophysique Interne et Tectonophysique (CNRS), Observatoire des Sciences de l'Univers, Université Joseph Fourier, Grenoble, France. Email: florence.renalie@obs.ujf-grenoble.fr; gregory.bievre@obs.ujf-grenoble.fr; denis.jongmans@obs.ujf-grenoble.fr; michel.campillo@obs.ujf-grenoble.fr; pierre-yves.bard@obs.ujf-grenoble.fr.*
[2]*Centre d'Études Techniques de l'Equipement de Lyon, Laboratoire Régional d'Autun, Autun, France.*

parameter for site characterization in current building codes (Finn and Wightman, 2003).

Various in situ methods can be applied to derive shear-wave velocity: borehole tests, shear-wave refraction and reflection studies, and surface-wave techniques (Jongmans, 1992; Dasios et al., 1999; Hunter et al., 2002; Boore, 2006). Borehole tests have been used extensively in geotechnical engineering to a depth of a few tens of meters. Such tests provide accurate and well-resolved V_S values with the following drawbacks: They are invasive, they are sensitive only to vertical variations of V_S, they are increasingly expensive with depth, and they offer only point estimates. Shear-wave velocities from noninvasive surface measurements can be obtained using transverse shear-wave (SH) refraction or reflection techniques (Dasios et al., 1999; Hunter et al., 2002; Ghose and Goudswaard, 2004). In a thick soil site in Canada, Hunter et al. (2002) applied high-resolution P and SH seismic reflection profiling to delineate the overburden-bedrock surface to a few hundreds of meters deep and obtained P- and S-wave velocities in the overburden layers from common midpoint (CMP) processing.

In recent years, surface-wave methods have been applied increasingly to measure V_S vertical profiles, using the dispersion properties of these waves (for a review, see Socco and Jongmans, 2004). Surface-wave methods commonly are divided into two main categories, depending on whether active or passive sources are used. Active methods record vibrations generated by an artificial source, a limitation of which is the difficulty to generate low-frequency waves (Tokimatsu, 1997). Consequently, active sources usually offer a penetration that is limited to a few tens of meters (Park et al., 1999; Socco and Strobbia, 2004).

On the contrary, ambient vibrations are generated by sources of lower frequencies (e.g., Aki, 1957; Satoh et al., 2001; Okada, 2003), thereby making active and passive techniques complementary to each other for deriving the surface-wave dispersion curve (Wathelet et al., 2004; Park et al., 2007; Richwalski et al., 2007; Socco et al., 2008). Thus, V_S profiles are estimated in two steps: (1) deriving the dispersion curve from the recorded seismograms (Lacoss et al., 1969) and (2) inverting the dispersion curve by using either direct search methods (Parolai et al., 2005; Dal Moro et al., 2007; Wathelet et al., 2008) or linearized inversion algorithms (Herrmann, 1987; Satoh et al., 2001).

Parallel to these developments, considerable interest has arisen during the past few years in the crosscorrelation of ambient seismic noise recorded at two distant receivers (Aki, 1957; Claerbout, 1968). Indeed, it has been demonstrated, both theoretically and experimentally, that such crosscorrelation converges (under certain conditions) toward the Green's function of the medium between these two receivers (Shapiro and Campillo, 2004; Schuster et al., 2004; Sánchez-Sesma and Campillo, 2006; Gouédard et al., 2008; Wapenaar et al., 2008). Because ambient seismic noise is produced mainly by surface sources that generate predominantly surface waves, that property can be used to map the surface-wave group velocity at different frequencies and to derive a 3D V_S image of a geologic structure, such as a 15- × 15-km-size volcano (Brenguier et al., 2007). Brenguier et al. (2007) also demonstrate that continuous ambient-noise records obtained over an 18-month period can detect very small seismic-velocity perturbations and can show decreases in seismic velocity before eruptions. At smaller scales, with interstation distances ranging between 50 and 500 m, recent studies have demonstrated the possibility of using ambient-noise crosscorrelation in an urban environment to retrieve the propagation functions (Nunziata et al., 2009) and to perform a 3D tomographic inversion for imaging shallow lateral heterogeneities (Picozzi et al., 2009).

The aim of the present paper is to show the benefit of using V_S to characterize and image landslides that affect clay masses, with a focus on the large Avignonet landslide (Trièves area, France). Following a discussion on the landslide and the measurements performed, we investigate the relation between V_S values and the damaging effect of this landslide at different scales, through laboratory and in situ tests. We then apply several active and passive seismic techniques at the Avignonet landslide to test the abilities of those methods to image a kilometer-size, 50-m-deep structure. Finally, seismic monitoring techniques are applied to crosscorrelated signals between two permanent stations, to detect changes in the medium that are related to the landslide activity during a three-year period of time.

The Avignonet Landslide: Geologic Context and Seismic Investigation

Geologic and geotechnical context

The large Avignonet slide (40×10^6 m^3) is located in the Trièves area (French Alps, Figure 1a). This 300-km^2 area is covered by a thick Quaternary clay layer (as thick as 200 m) that was deposited in a lake dammed by a glacier during the Würm period (Giraud et al., 1991). Those clayey deposits overlie compact old alluvial layers and marly limestone of Mesozoic age and are covered by thin till deposits. After the glacier melted, rivers cut deeply into the geologic formations, triggering numerous landslides

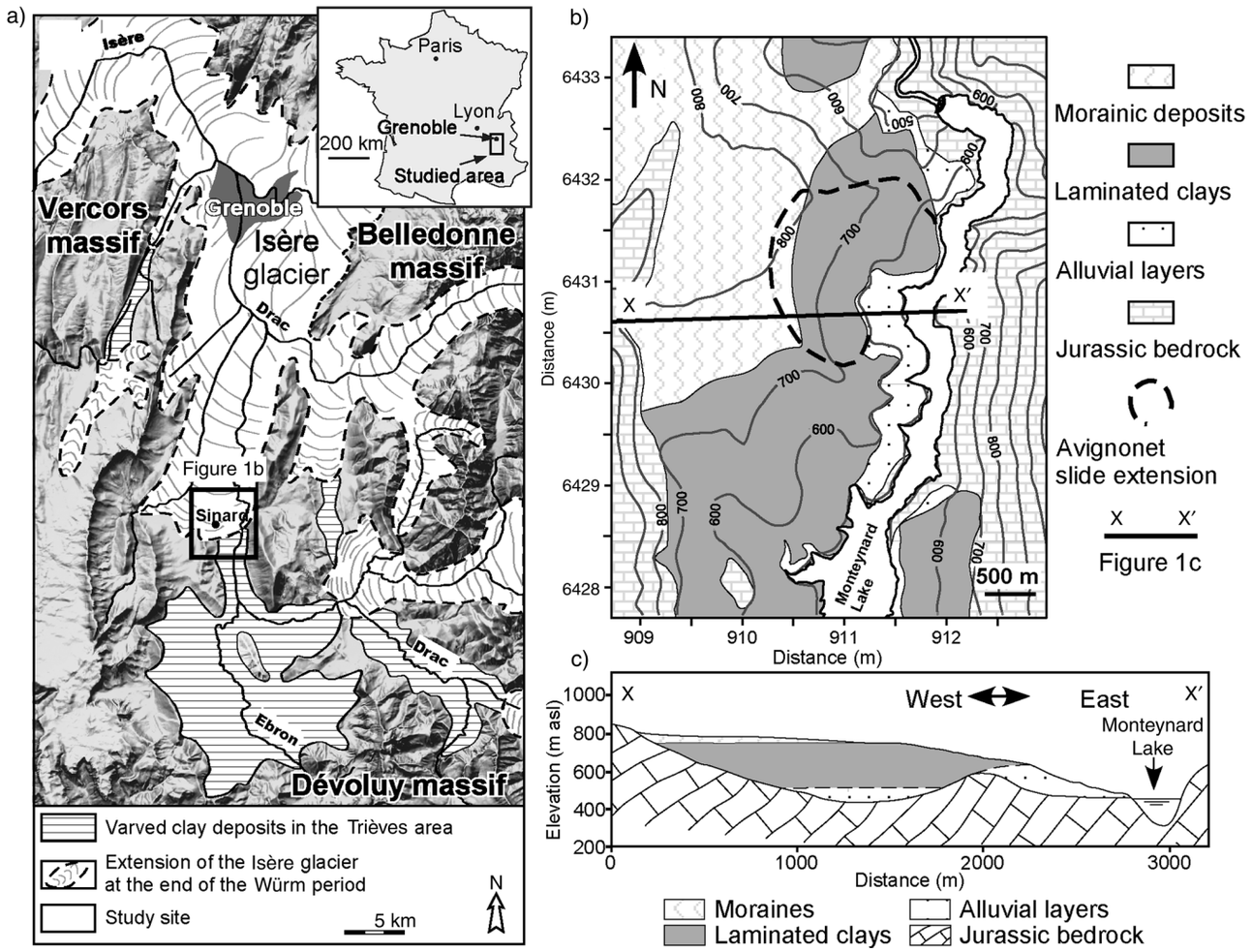

Figure 1. (a) Location map of the Trièves area and of the study site. (b) Geologic map of the study area, with the location of the Avignonet landslide (dashed line) and section XX′. (c) Geologic cross section XX′.

(Giraud et al., 1991). Figure 1b shows the simplified geologic map of the study area, in the northern part of the Trièves region, with the extension of the Avignonet landslide having occurred in the clay deposits. An east-west synthetic geologic section over the Avignonet landslide is presented in Figure 1c, showing the westward increase in thickness of the clay layer, from 0 m to more than 200 m.

The Avignonet landslide has been investigated by geologic, geotechnical, and geophysical tests since the beginning of the 1980s. Giraud et al. (1991) and Jongmans et al. (2009) provide a summary of the results. Five boreholes (labeled B0 to B4) were drilled in the southern part of the landslide (Figure 2), where a hamlet is settled. Table 1 synthesizes the geologic logs and the detected slip-surface depths. The contact between the clay and the underlying alluvial deposits was found at 14.5 m, 44.5 m, and 56 m in B2, B3, and B1, respectively.

On the contrary, B0 and B4 only encountered clay deposits, in agreement with the westward thickening of this clay formation. Inclinometer data and geologic logs have revealed at least three rupture surfaces: a shallow one at a few meters in depth, an intermediate one at 10–16 m, and a deep one at 42–47 m. Water-level measurements showed the presence of a very shallow water table (1 to 3 m below the ground level). The Avignonet slide has been monitored by biannual GPS measurements at 26 geodetic points since 1995. The velocity values averaged from the available GPS measurements were used to identify areas of increasing slide velocity (Figure 2). Slide velocities have varied from 0 to 2 cm/yr at the top of the slide, to 7 to 15 cm/yr in the most active parts, around boreholes B2 and B4 (Jongmans et al., 2009). Most of the area is sliding southeastward, parallel to the general slope.

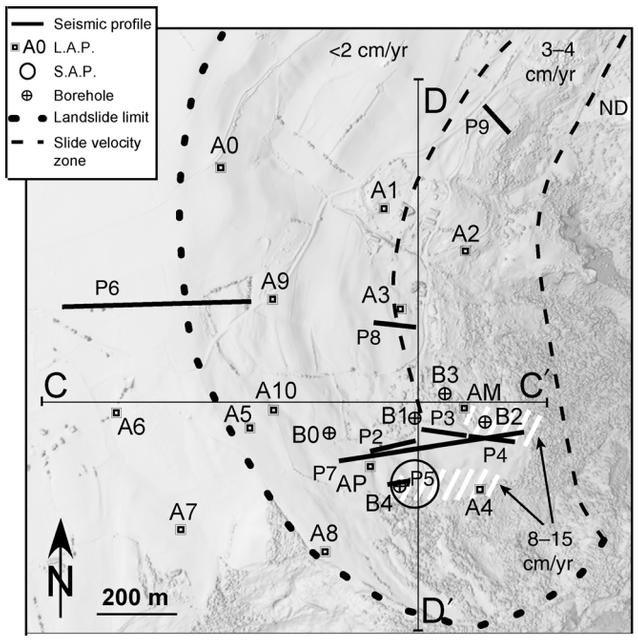

Figure 2. Locations of tests on the Avignonet landslide (delineated with a dotted line). Seismic profiles are labeled P2 through P9. Profile P1 is outside the represented area, about 300 m west of the top of the figure. Boreholes are labeled B0 through B4. Seismological stations of the large-aperture network (L.A.P.) are A0 through A10. There are two permanent stations: AP and AM. The circle encompasses the small-aperture network (S.A.P.). There are three zones, with different displacement rates (ND has no displacement, <2 cm/yr, and 3–4 cm/yr), and they are delineated by dashed lines, whereas very active areas (7–15 cm/yr) are indicated with white hatching. Sections CC′ and DD′ refer to the two sections shown in Figure 9.

Seismic investigation

The Avignonet landslide has been investigated recently via several geophysical campaigns. The first geophysical survey was performed in 2006–2007 (including seismic profiles P1 through P4, P6, and P7 in Figure 2) to test the sensitivity of three geophysical parameters (the electrical resistivity ρ, the seismic P-wave velocity V_P, and the S-wave velocity V_S) to the deformation resulting from the slide. It turned out that in such saturated clays, ρ and V_P are influenced strongly by the water level and are affected little by the landslide activity (Jongmans et al., 2009). On the contrary, V_S showed significant variations both vertically and laterally that correlated with the landslide activity. For this reason, we have focused the present study on V_S measurements.

Additional seismic profiles P5, P8, and P9 (Figure 2) were conducted in 2008–2009. Except for profiles P6 and P7, seismic profiles were performed using 24 vertical geophones (4.5 Hz) and 24 horizontal geophones (4.5 Hz for P5 and 14 Hz for all other profiles) spaced 5 m apart (2.5 m for profile P5), with a hammer striking a plate or a plank for the source, to record Rayleigh waves and SH-waves, respectively. Given the V_S values in the medium, these geophone spacings did not alias the data spatially. Shots were located at every third geophone for the purpose of seismic tomography, and with offset at both ends for the surface-wave recordings. The two 470-m-long profiles P6 and P7 were conducted with 48 vertical geophones (resonance frequency 4.5 Hz) at a 10-m spacing. Signals were generated by nine and 14 explosive sources with an 80-m spacing and a 50-m spacing, respectively. Depending on the accessibility of the area, one or two offset shots were fired at each end.

In addition, three concentric arrays composed of six 5-s three-component seismometers were installed successively in 2007 close to profile P5 (see Figure 2 for location). Each array was composed of five Lennartz 5-s sensors distributed regularly around the same central sensor, with an increasing radius of 20 m, 40 m, and 60 m. Ambient vibrations were recorded during one hour for each array. Finally, a large-aperture array (kilometer size) of eleven short-period seismological stations A0 to A10 (Figure 2) were installed during two weeks in 2007 on the southern part of the Avignonet landslide, which also is equipped with two permanent stations AP and AM (OMIV observatory: www-lgit.obs.ujf-grenoble.fr/observations/omiv).

Evolution of Clay Damage Inferred from V_S

A previous study on the V_S value distribution along a section through the Avignonet landslide (Jongmans et al., 2009) showed an inverse relation between V_S and displacement rate. Considering additional data acquired in 2008 and 2009 (profiles P5, P8, and P9), V_S values measured at a depth of 10 m versus displacement rate are plotted in a semilogarithmic scale in Figure 3a. The point outside the landslide exhibits no measurable displacement and is represented as a bar with a maximum displacement rate of 0.01 cm/year. Data show a strong decrease of V_S values with increasing displacement rates, from 630 m/s outside the slide to 225 m/s at the slide toe, where the ground surface is the most disturbed. These results obtained for meter-scale wavelengths suggest that the gravitational deformation strongly affects the shear-wave velocity in the clay.

The results are interpreted as the effect of an intensive cracking of the material at different scales, resulting from

Table 1. Geologic log and depth of the slip surfaces found in boreholes B0 through B4 (shown in Figure 2).

Borehole #	Depth (m)	Geologic log	Shallow slip surface (m)	Intermediate slip surface (m)	Deep slip surface (m)
B0	89	0–5 m: morainic colluvium 5–89 m: laminated clays	5	10	47
B1	59	0–5 m: morainic colluvium 5–56 m: laminated clays 56–59 m: alluvial deposits	×	15	43
B2	17	0–4 m: morainic colluvium 4–14.5 m: laminated clays 14.5–17 m: alluvial deposits	1.5 and 4	12	×
B3	59	0–4 m: morainic colluvium 4–44.5 m: laminated clays 44.5–59 m: alluvial deposits	×	16.5	×
B4	49	0–2.5 m: morainic colluvium 2.5–18.5 m: blocky clays 18.5-49 m: laminated clays	5	10.3 and 14.5	42

Note: The inclinometer tube within B3 was sealed to a depth of 20 m. Dashes indicate that the presence of a slip surface at that depth was not shown during the time of the inclinometer measurements, which does not imply that a slip surface does not exist.

slip along the rupture surfaces at different depths. This cracking probably increases the void ratio and, consequently, increases the water content in the saturated material and also decreases the shear-wave velocity. Relations among V_S (or shear modulus), void ratio, and mean effective stress have been derived from numerous laboratory studies for a wide variety of soil types (e.g., Bryan and Stoll, 1988). For a given depth (fixed confining pressure), they show that V_S effectively decays with increasing void ratio. For increasing confining pressures, the laws predict an increase in shear-wave velocity, which still depends on the void ratio.

To investigate the relation among V_S, void ratio, and confining pressure in the clay of the Avignonet landslide, we performed laboratory measurements on three 0.4-m-long saturated soil specimens (two laminated, one nonlaminated) sampled during drilling at 8.3 m, 9.8 m, and 15.5 m in two different boreholes. Clay specimens were submitted to isotropic stress conditions in a triaxial cell, with confining pressures varying between 0 and 400 kPa. With the low V_S/V_P values (0.1 to 0.2) found in the landslide (Jongmans et al., 2009), Poisson's ratios are higher than 0.48 and horizontal effective stresses are close to the vertical effective stress. Confining pressures ranging between 0 and 400 kPa then approximately correspond to depths ranging between 0 and 40 m in saturated conditions.

Measurements of V_S were made under saturated conditions using a GDS instrument associated with bender elements (Lee and Santamarina, 2005). Signals were generated at a frequency of 10 kHz and yielded a wavelength of about 0.7 to 3 cm. The volume, weight, and water content of the saturated samples were measured before introducing them into the cell, and the void ratio was derived from the water volume expelled during the experiment. Figure 3b shows the evolution of V_S with the void ratio and the corresponding water content in the 0- to 400-kPa confining-pressure range. In the investigated void-ratio range, V_S values exhibit a significant and regular decrease with increasing void ratio e (and decreasing confining pressure p), from 300 m/s for $e = 0.52$ ($p =$ 400 kPa) to 70 m/s for $e = 0.92$ ($p = 0$ kPa). These values will be compared later with the shear-wave velocities derived in situ in the depth range of 0 to 40 m.

Active Methods

A 17-m-deep downhole test performed close to borehole B4 (Figure 2) in a highly disturbed area provided the V_S vertical profile shown in Figure 4. The V_S values in the first 3 m were obtained from Love-wave fundamental-mode velocities (see below). The V_S increases from less than 150 m/s in the shallow layer to more than 300 m/s at the bottom of the profile, with two velocity breaks at 6 m and 15 m. These depths approximately fit two slip surfaces found in borehole B4 (Table 1). At 10 m deep, V_S is approximately 250 m/s, which confirms the activity of the landslide at this site (Figure 3a).

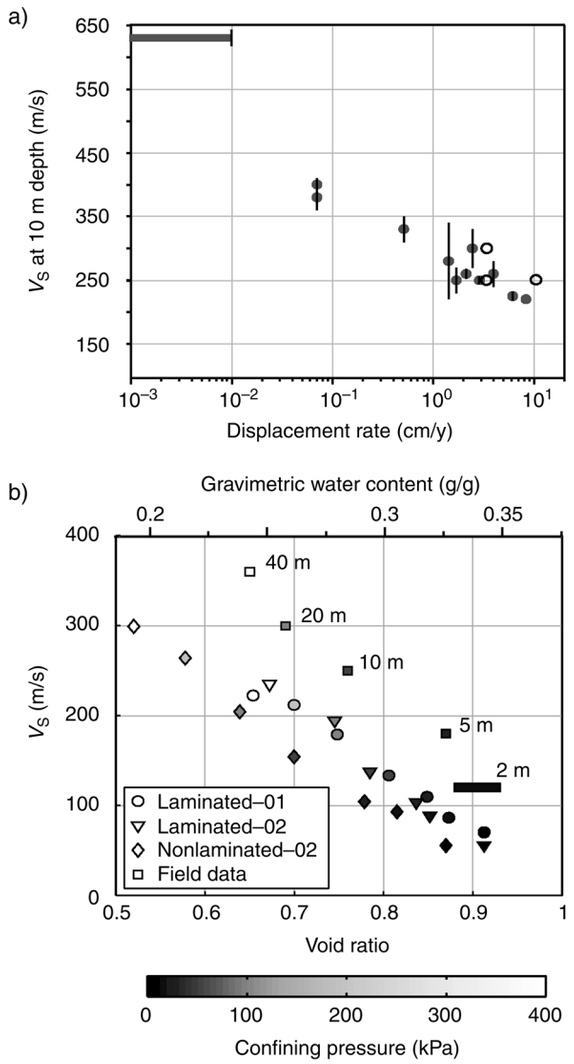

Figure 3. Measured *V*s variations. (a) Evolution of shear-wave velocity values (with error bars) as a function of displacement rates, at a depth of 10 m. Data are from surface-wave inversion and SH refraction studies for the profiles shown in Figure 2. The three empty circles correspond to the new measurements. The point outside the landslide ($V_S = 630$ m/s) exhibits no measurable displacement and is represented as a thick line with a maximum displacement rate of 0.01 cm/year. (b) Evolution of V_S as a function of void ratio and water content for three saturated samples and field data. The shaded scale indicates the confining pressure. Modified from Bièvre et al. (2010).

Shear-wave velocity also can be measured from the surface by using active sources, with surface-wave methods or with transverse-shear-wave (SH) refraction or reflection techniques. The penetration depth of SH refraction tests usually is limited to 25–30 m because of the difficulty of generating SH-waves with a good signal-to-noise ratio over distances greater than 100 m (Jongmans et al., 2009). Figure 4a shows the 57.5-m-long SH refraction tomography profile P5, recently performed in the highly disturbed zone where borehole B4 was drilled and where the downhole test discussed in the previous section was conducted. The tomography (Dines and Lyttle, 1979) was performed on a grid that was 2.5 × 2.5 m, starting from a three-uniform-layer model derived from the classical refraction analysis. The seismic image shown in Figure 4a, with a least-squares misfit of $<3\%$ between measured and calculated traveltimes, was obtained after five iterations, after which the misfit remained stable.

The V_S profile obtained from a downhole test is plotted in the same figure. Because signals were difficult to pick in the first 3 m, we constrained V_S values close to the surface from Love-wave velocities along profile P5. Figure 4b and c shows the Rayleigh- and Love-wave dispersion curves, respectively, computed for a group of 15 geophones centered above B4. In the same figure, the normalized amplitudes of the smoothed Fourier spectra also are plotted. The Rayleigh waves (Figure 4b) are dominated by a higher mode in the 18- to 25-Hz frequency band, thereby preventing us from identifying the fundamental mode at these frequencies. On the contrary, the fundamental mode dominates the Love waves (Figure 4c) over the whole frequency range, including values greater than 20 Hz, where its velocity corresponds to V_S in the upper layer. Thus, the V_S profile derived from borehole measurements was completed with this V_S value in the first 3 m.

Downhole measurements and SH-wave refraction tomography show consistent results (Figure 4a), with a surficial low-velocity layer (V_S lower than 200 m/s) over the shallow slip surface found at 5 m. In the depth range between the shallow and intermediate slip surfaces (5–15 m), V_S is approximately 250–300 m/s and increases to 400 m/s below the intermediate slip surface. The SH-wave refraction tomography provides the lateral variations in velocity, highlighting the eastward thickening of the shallow low-velocity unit (lower than 150 m/s, Figure 4a). On the other hand, this technique is unable to provide an image down to the deepest slip surface of the landslide, which was found at 42 m in borehole B4.

The surface-wave inversion technique at a larger scale has been applied already to the slowly moving parts of the Avignonet landslide (Jongmans et al., 2009), which contributed to the results of Figure 3a. Here we investigate the possibility of inverting Rayleigh waves measured along the 470-m-long profile P7, which is oriented perpendicularly to the landslide motion and extends in the lower and more active part of the landslide. The first ten geophones are located in this highly sliding velocity zone (Figure 2,

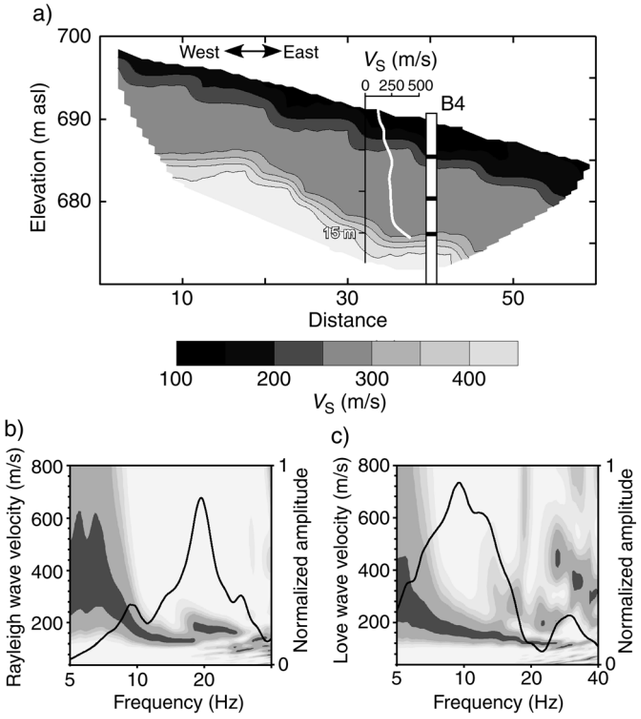

Figure 4. (a) SH refraction tomography along profile P5 (located in Figure 2), performed with a three-uniform-layer initial model inferred from classical refraction analysis and a grid that is 2.5 m on each side. The misfit is 2.4%. The V_S profile derived from the combination of downhole test and inversion of Love waves is plotted in the same figure, as is borehole B4 with the shallow and two intermediate slip-surface positions. (b) Rayleigh-wave and (c) Love-wave dispersion maps with normalized Fourier spectra of signals recorded at B4. The Love-wave dispersion curve was used for constraining V_S values of the downhole test in the first 3 m.

and group A in Figure 5a), which is characterized by low V_S values and a rugged topography resulting from active surficial rupture surfaces. Figure 5a shows the seismograms recorded for a shot at 470 m (upper end of the profile) using 200 g of explosive. Surface waves are regular from 470 m to 80 m, but they exhibit attenuation and disturbances in the active area from 80 m to 0 m, making any determination of dispersion curves difficult in this high-scattering medium.

Ground heterogeneity caused by the landslide activity also might affect the applicability of the surface-wave method along a linear array outside the disturbed zone. Several methods were proposed (Miller et al., 1999; Grandjean and Bitri, 2006; Lin and Lin, 2007; Socco et al., 2009) for obtaining pseudo-2D V_S images from local 1D surface-wave inversion, using different source-receiver layouts. The main assumption is that locally the structure is layered horizontally (1D) around a receiver antenna (Grandjean and Bitri, 2006) or between one receiver and some shots (Lin and Lin, 2007). To test this hypothesis, we considered a group of 20 geophones located on P7 outside the disturbed area (from 200 to 400 m, group B in Figure 5a) and we applied the frequency-wavenumber (*f-k*) analysis (Lacoss et al., 1969) to transform the data from the time-space domain into the frequency–phase velocity domain (dispersion map), from which dispersion curves can be extracted.

Figure 5 shows the seismograms for three shots, at 0 m, 100 m, and 450 m (Figure 5c, d, and e), together with the dispersion maps for these three shots and three additional ones (50 m, 150 m, and 570 m, Figure 5f through k). The Fourier spectrum of the signal in the center of the geophone spread also is shown in these graphs, revealing the filter effect of the geophones below 4 Hz. For shots located in the upper part of the profile (450 m and 570 m), Rayleigh waves propagate regularly through the geophone array and the dispersion curve of the fundamental mode is clearly defined between 3 Hz and about 10 Hz, with phase velocities decreasing from 400 m/s to 200 m/s. Higher modes seem to have been excited in some limited-frequency bands. The upper frequency limit of 10 Hz corresponds to the aliasing criterion ($\lambda_{min} = 2\ \Delta x$, where Δx is the 10-m geophone spacing). On the other side of the spread, for the two shots fired in the lower active zone (0 and 50 m, Figure 5f and g), the first higher mode is excited at least as much as the fundamental mode, which cannot be identified clearly. Moreover, the signal duration is much longer than for sources located in a less-disturbed area (compare seismograms in Figure 5c and d). For shot positions outside the very disturbed area (Figure 5h and i), the fundamental mode of Rayleigh waves again is well defined. Figure 5b shows the dispersion curves extracted for shot positions outside the very disturbed area (at $x > 100$ m), on both sides of the geophone array (which is between $x = 200$ m and 400 m). They are all similar in the 3- to 10-Hz frequency range, thereby highlighting the 1D geometry of the seismic ground structure below the spread. On the contrary, late arrivals on the seismograms of shots performed in the very disturbed area can be compared to coda waves, which result from scattering on seismic heterogeneities (Aki and Chouet, 1975; Aki and Richards, 1980).

Furthermore, higher modes may be excited in the case of inversely dispersive media for particular source-to-receiver distances (that can be determined theoretically; Tokimatsu et al., 1992), and in the case of deep sources or in the case of deep heterogeneities along the wave path (Herrmann, 1973; Keilis-Borok, 1986; Schlue and Hostettler, 1987;

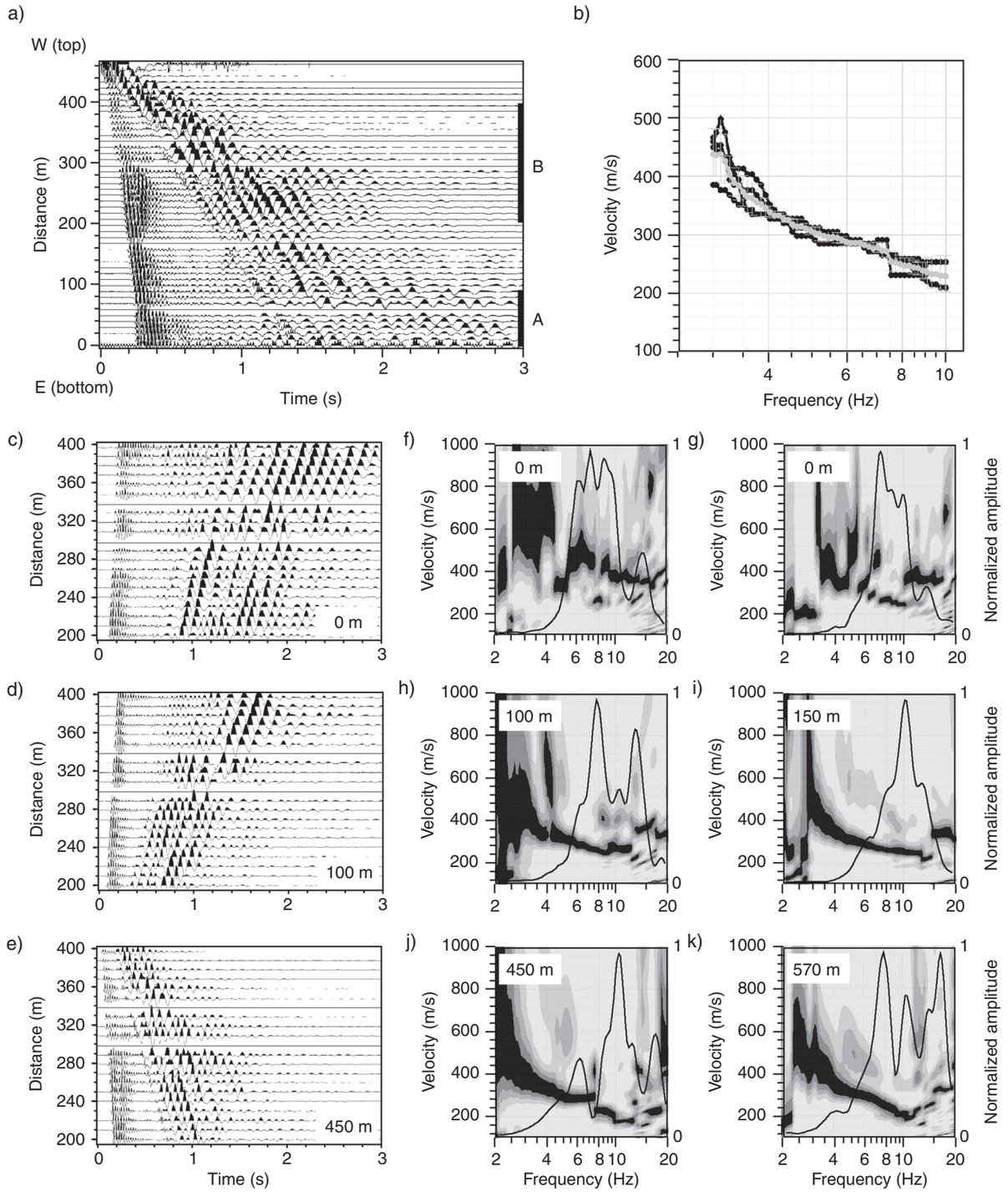

Figure 5. Active-source (explosive) experiment along profile P7. (a) Normalized signals recorded along profile P7 for the offset shot at 470 m. Vertical geophones are 10 m apart. The two groups of geophones located in the very-disturbed and less-disturbed areas are labeled A and B, respectively. (b) Dispersion curves extracted from the dispersion maps of Figure 5h–k, for shot positions greater than 100 m. Gray curve is the average. (c)–(e) Seismograms recorded by geophones of group B (200 m to 400 m) for shots at 0 m, 100 m, and 450 m, respectively. (f)–(k) Dispersion maps for shots at 0 m, 50 m, 100 m, 150 m, 450 m, and 570 m, respectively. Normalized Fourier spectrum of the signal recorded at 290 m is plotted on each dispersion map.

Uebayashi, 2003). In our case, excitation of the first higher mode only occurs for shots performed in the disturbed area and not on the other side of the geophone array. Moreover, borehole measurements indicated a normally dispersive medium. Both the long duration of signals and the excitation of the first higher mode on seismograms generated in the disturbed area therefore probably are related to waves scattered on seismic heterogeneities linked to the landslide activity (scarps, open fissures, lateral velocity variations).

In the disturbed zone, the presence of scatterers in and out of the propagation plane turned out to make the use of the surface-wave method with linear arrays difficult. This conclusion also was reached during a seismic survey carried out on the large Séchilienne landslide affecting mica schists (Méric et al., 2005). These scatterers, which blur the dispersion curve here, can help to retrieve it when nonlinear arrays and ambient vibrations are used, however.

Passive Methods

Small-aperture array

Dispersion curves determined on long linear arrays with active sources (Figure 5b) are limited to 3 Hz in the low-frequency range, as a result of the low-cut filter effect from the 4.5-Hz geophones, combined with the source energy spectrum. The maximum penetration depth then is about 30 m, considering the rule of the thumb of one-third of the maximum wavelength. That penetration is not enough to reach the deepest slip surface of the landslide, which was found at a depth between 42 and 47 m in boreholes (Table 1). To obtain the dispersion curve at lower frequencies, we used surface-wave inversion of ambient vibrations recorded with an array of sensors (Asten and Henstridge, 1984; Satoh et al., 2001).

The main assumptions behind noise-array analysis are that ambient vibrations are composed mostly of surface waves and that the ground structure is stratified approximately horizontally (Tokimatsu, 1997). The geometry of the three concentric arrays (radii of 20, 40, and 60 m) is shown in Figure 6a. We applied the *f-k* method proposed by Lacoss et al. (1969), which assumes that plane waves travel across the array of sensors. The maximum output of the array is calculated by the summation, in the frequency domain, of signals shifted according to the time delays at the sensors. To estimate the uncertainty of the determination of apparent velocity at each frequency, signals are split into several short time windows (50 periods in this case), for each of which the output of the array is computed. Following Ohrnberger et al. (2004), a histogram of the velocities at the observed maxima is constructed for each frequency band, thereby allowing determination of the dispersion curve. The low- and high-frequency limits of the dispersion curve are controlled by several factors, including the maximum and minimum apertures of the array, filter effect of the medium, and excitation strength of the wavefield (Scherbaum et al., 2003). Resolution and

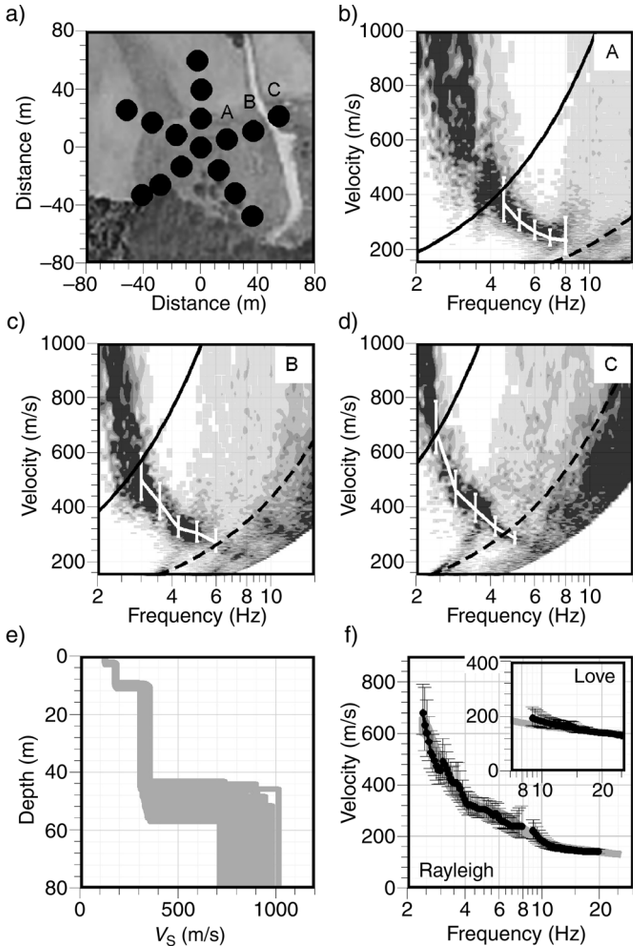

Figure 6. Surface-wave inversion. (a) Geometry of the three concentric arrays (A through C), composed of six 3-C seismometers with radius of 20 m, 40 m, and 60 m, plotted on top of an aerial photograph of the area. (b)–(d) Frequency-wavenumber analysis for arrays A through C. Continuous and dashed lines represent the resolution (continuous) and aliasing (dashed) limits of the dispersion curves. (e) Four-layer V_S profiles with a misfit lower than 1. (f) Rayleigh (main plot) and Love (inset) dispersion curves. Black line: dispersion curve measured from passive (2.4–8 Hz) and active (9–18 Hz and 9–25 Hz for Rayleigh and Love waves, respectively) seismic experiments. Gray lines depict theoretical dispersion curves of profiles in (e).

aliasing limits (related to the geometry of the array) are derived from the array-response study (Wathelet et al., 2008). The resulting velocity histograms are shown in Figure 6b, c, and d for the three arrays A, B, and C, respectively, along with the resolution and aliasing limits. The final dispersion curve, with the associated uncertainty, is presented in Figure 6f (black lines) and was completed at high frequencies with the Rayleigh and Love dispersion curves derived from profile P5 (Figure 4b). With the characteristics of the array, the Rayleigh dispersion curve obtained from ambient vibrations is reconstructed between 2.4 and 8 Hz and is complementary to the one derived from active seismics between 9 and 18 Hz. Although the frequency band is extended only slightly toward low frequencies compared with dispersion curves derived from large-scale active seismics (2.4 Hz for array C instead of 3 Hz for profile P7; see Figure 5), the ambient-noise analysis caught the increase of slope and reached a phase velocity of 680 m/s at 2.4 Hz, yielding a wavelength of about 280 m and a penetration greater than 90 m. Reaching as high as 25 Hz, the Love-wave dispersion curve measured on the small seismic profile P5 moreover gives information on the very shallow part of the profile. The parameterization chosen for the inversion was a model with a surficial layer of 3 m maximum and three other homogeneous layers, as suggested by previous investigation. Within the uncertainty of the data, all shear-wave velocity profiles explaining the data are given in Figure 6e. In agreement with the results of the SH refraction tomography, the surficial layer has a very low velocity, between 120 and 140 m/s. Values of V_S between 160 and 200 m/s and depth values ranging between 8 and 12 m characterize the second layer, which corresponds approximately to the highly disturbed horizon overlying the intermediate surface ruptures found between 10 and 14.5 m in borehole B4 and shown in the downhole test (Figure 4a). The third layer, with a velocity below 400 m/s, extends to a depth between 40 and 60 m and overlies a stiffer layer with V_S values higher than 700 m/s. This interface probably corresponds to the deepest slip surface, which was found between 42 and 47 m in boreholes.

In situ measured V_S values at 2, 5, 10, 20, and 40 m are plotted in Figure 3 against the void-ratio values determined in the borehole at the same depth. Compared with laboratory measurements, in situ V_S values exhibit a similar linear decrease with increasing void ratio, for the same depth range. The covered velocity range is higher (from 120 to 360 m/s) than the laboratory measurements (70 to 300 m/s), which indicates that soil samples could have been remolded during extraction. Nevertheless, these results suggest that the clay material is probably as strongly damaged at the centimeter scale as it is at the meter scale, thus highlighting the penetrative characteristic of the cracking generated by the landslide activity. Comparison of Figure 3a and b also shows that the V_S variation resulting from landslide damaging (at a given depth) is as strong as the one expected from the landslide surface to its bottom. Although V_S variations probably also are affected by other factors, such as stress, cementation, or granularity, these results again highlight geoscientists' interest in using V_S for imaging a clay landslide.

It has been shown that surface-wave inversion from ambient vibration measurements can provide locally valuable information on the velocity structure of a 50-m-deep landslide such as the Avignonet landslide. However, constraining the geometry of the entire landslide would require at least 100 arrays (ome point every 100 m) for constructing a 3D model. The time necessary to cover the whole area by moving such arrays has been estimated to be about three months of work, with a team of three people, when considering the problems of forested and built areas. For that reason, we investigated the possibility of performing a surface-wave tomography on the landslide, by retrieving wave-propagation times between stations using crosscorrelation of ambient noise. Our aim is to test the capacity of the technique to obtain a first-order 3D model of the landslide, using a limited number of sensors.

Large-aperture array

We applied the crosscorrelation technique to the records of the large-aperture network (kilometer size) of 13 seismological stations installed on the southern part of the Avignonet landslide (A0 to A10, and AP and AM, in Figure 2). To evaluate the quality of the propagation functions computed from crosscorrelation of ambient noise, explosive shots were performed close to each station. The direct and crosscorrelated signals involving station A2 were band-pass filtered between 2 Hz and 4 Hz and the results are plotted in Figure 7a. The waveforms of the direct and correlated signals are not strictly equal because of differences in their frequency content. However, arrival times and waveforms of the most energetic wave (the direct Rayleigh wave) are comparable, showing the reliability of the crosscorrelation technique for reconstructing the Rayleigh-wave propagation between stations. In the same figure are shown the Rayleigh-wave dispersion maps (group velocity) computed by using the S-transform (Stockwell et al., 1996) for the propagation from A2 to A0. On the shot image (Figure 7b), the fundamental mode of the Rayleigh wave can be picked between 3 Hz and

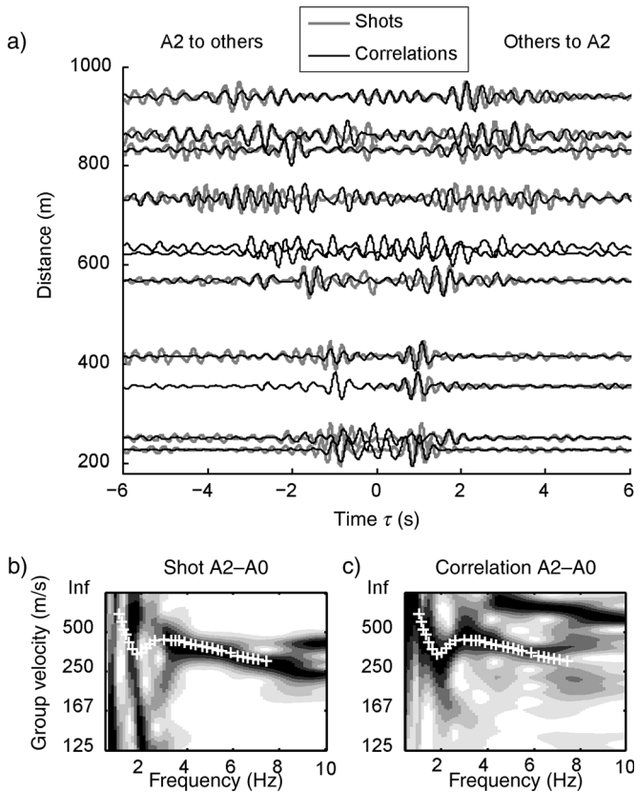

Figure 7. Ambient-noise crosscorrelation. (a) Comparison of the direct-shot signal (gray shading) and the noise-crosscorrelated signal (black shading) between A2 and the other stations in the 2- to 4-Hz frequency band. (b) Shot dispersion image computed for propagation from A2 to A0, and (c) crosscorrelation dispersion image computed for propagation from A2 to A0. The white crosses in (b) and (c) indicate the dispersion curve picked from the comparison of the two images.

10 Hz, whereas it can be determined in the 1.5- to 5-Hz-frequency range on the crosscorrelation image (Figure 7c). The high-velocity mode observed between 4 and 10 Hz is visible only for this couple of stations and therefore cannot be used in the following part of the study.

On the whole network, noise crosscorrelations and shots gave complementary information on the Rayleigh fundamental mode. They were combined to obtain path-averaged (averaged over the path between two stations) group-velocity dispersion curves that cover the 1.5- to 7-Hz frequency range for the different pairs of stations. Interestingly, the frequency range for shots is similar in Figure 5 (a 470-m-long seismic profile with 4.5-Hz geophones) and 7 (a kilometer-size network with short-period seismological stations), showing that the low-frequency limit of the dispersion-curve frequency is controlled mainly by the frequency content of the source.

A tomographic inversion was performed on the arrival-time measurements given by the Rayleigh group-velocity dispersion curves, using the algorithm of Barmin et al. (2001). This simple algorithm considers straight rays on a regular grid. It includes a spatial smoothing, and it also includes a constraint on the amplitude perturbation that depends on local path density. The 15-cell by 15-cell tomographic grid was 100 m long on each side. Because of the sparse ray coverage, we chose to give great importance to the spatial-smoothing parameter (Brenguier et al., 2007). Thus, a group-velocity map was obtained for frequencies between 1.5 and 7 Hz, using measurements at 0.1-Hz intervals. Figure 8a and b shows the maps for 1.7 and 4 Hz, together with all paths on which dispersion curves could be picked at these frequencies. These group-velocity maps highlight two different features of lateral variations at high and low frequencies. The reliability of these results was evaluated using checkerboard tests with heterogeneities of various sizes (Figure 8c through f). The lateral variations are well reconstructed within the array, but their shapes are smoothed and their amplitudes are attenuated as a result of the smoothing parameter.

In addition, local group-velocity dispersion curves were reconstructed for each cell of the surface model. Each of those curves then was 1D inverted both for V_S and thickness values with a neighborhood algorithm (Sambridge, 1999; Wathelet, 2008), using a parameter space that defined four layers over a half-space (Renalier, 2010). To reconstruct a 3D V_S model of the area, we then computed for each cell the average of all resulting V_S profiles that had a misfit smaller than 1.2 times the minimum misfit. In the following, we focus on the results and their comparison with those of other V_S imaging techniques.

Figure 9 shows two perpendicular cross sections (CC′ and DD′) made through the 3D V_S structure. The east-west cross section CC′ intersects boreholes B0 through B3, whereas the south-north section DD′ crosses boreholes B1 and B4. The headscarp and the slip surfaces found in boreholes also are located in Figure 9. The depth of the deep slip surface (found between 42 and 47 m, Table 1) correlates very well with the 400-m/s velocity contour at which a vertical contrast is observed in both Figures 6 and 9. The landslide body appears to be characterized by a velocity V_S lower than 400 m/s, and it thins significantly down to the west, in agreement with the headscarp location (Figure 9a). A regular thinning of the landslide body from 40 m to 20 m also is observed to the north (Figure 9b), but no geotechnical data are available for this area. Within the landslide mass, another vertical V_S contrast can be seen at a depth of about 15 m, which correlates

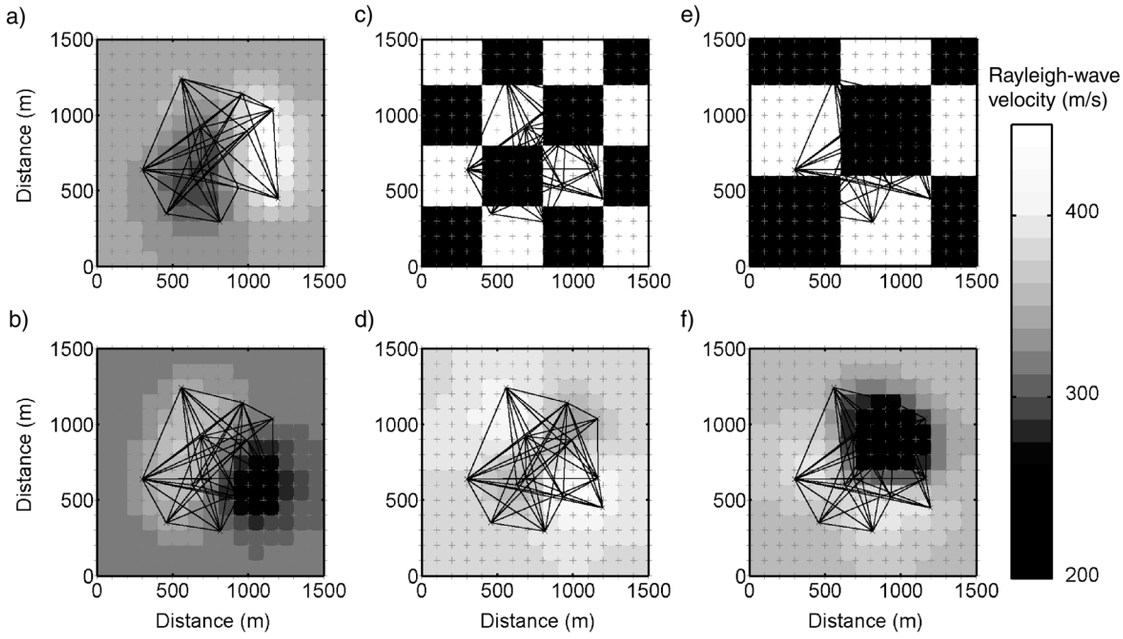

Figure 8. Group velocity maps resulting from the tomographic inversion: (a) at 1.7 Hz, and (b) at 4 Hz. Black lines indicate the available ray coverage at the corresponding frequency. (c) Checkerboard test with 400-m-side lateral heterogeneities and the ray coverage available at 4 Hz. (d) Group velocity map obtained from inversion of synthetic traveltimes computed from the model of (c). (e) Checkerboard test with 600-m-side lateral heterogeneities and the ray coverage available at 4 Hz. (f) Group velocity map obtained from inversion of synthetic traveltimes computed from the model of (e).

well with the intermediate slip surfaces detected in the boreholes (Table 1) and by the active seismic experiments (Figure 4). However, that depth is near the minimum penetration that is related to the maximum frequency of 7 Hz. Finally, the faster velocities at depths below boreholes B1 through B3 hint at the shallow presence of compact alluvial layers and Jurassic bedrock. Further, the velocities of those alluvial layers and bedrock are underestimated because of the tomographic smoothing and the poor ray coverage at low frequencies in that area, which also explain the slight difference in V_S values measured at depth with the small-aperture array.

This surface-wave inversion from a combination of ambient-noise crosscorrelation and explosive shot signals agrees well with independent geotechnical and geophysical results, which proves the potential of such a technique for imaging deep-seated landslides that affect clayey deposits, even in a rural environment. Further improvements could be obtained by using (1) more stations for a better ray coverage, (2) longer recordings for reconstructing the propagation functions at higher frequencies from noise correlation, or (3) specific processing techniques for reconstructing those propagation functions, even in the case of directional noise (Roux, 2009).

Landslide Monitoring

Because landslide characterization also includes a temporal dimension, we tested the ability of the crosscorrelation technique to monitor evolution of material degradation related to gravitational movement. For this purpose, we used the continuous seismic data available at the two permanent stations, AP and AM (Figure 2), from October 2006 to May 2009. Unfortunately, numerous gaps were present in the data, as a result of material robberies and of malfunctions.

After spectral whitening of the one-hour noise signals (sampled at 125 Hz), crosscorrelation functions were computed in three frequency ranges (1.3–3.5 Hz, 2–5 Hz, and 5–10 Hz) and summed to obtain one-day crosscorrelation functions (Figure 10, left column). In the same figure (right column) are continuous plots of 12 12-day correlations whose dates are indicated on the left axis. In the two lowest-frequency ranges, 1.3–3.5 Hz and 2–5 Hz (Figure 10a through d), correlations are stable, with coherent arrivals as high as 10 s (especially at $\tau = -7$ s for both frequency bands). However, correlations at low frequencies (1.3–3.5 Hz) are asymmetrical, which indicates an anisotropic distribution of the noise (Stehly et al., 2006). In the

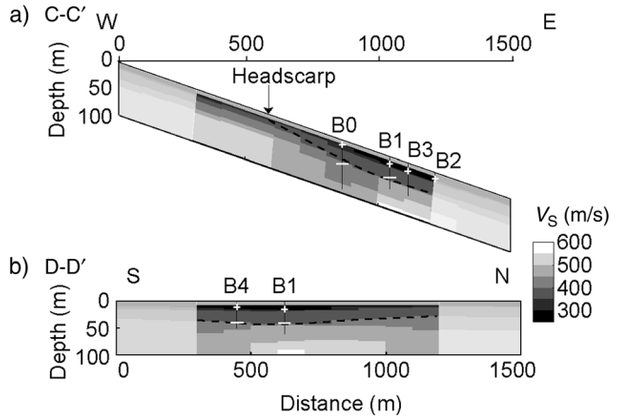

Figure 9. V_S images resulting from inversion along sections CC′ and DD′ (see locations in Figure 2). (a) Parallel to the slope; the depth scale is exaggerated 2×. (b) Perpendicular to the slope. Deep and intermediate slip surfaces found in boreholes B0 through B4 are indicated by crosses and horizontal bars, respectively. Shaded areas on top and on both sides indicate low resolution.

high-frequency band (5–10 Hz), signals are asymmetrical and propagation functions are reconstructed only during the first 1 to 2 s, after which the different arrivals are less stable.

Next, the signals in the three frequency bands were processed, looking for temporal variations in the wave propagation. We used two methods for measuring the relative variations of the velocity $\Delta V/V$ during the period studied — the doublet technique (Poupinet et al., 1984; Brenguier et al., 2008) and the stretching technique (Sens-Schönfelder and Wegler, 2006; Hadziioannou et al., 2009). These two techniques rely on the hypothesis that observed waveform fluctuations result only from a homogeneous variation in seismic velocity in the medium. In such a case, the relative traveltime shift $\Delta\tau$ between the perturbed and reference correlations is proportional to the time-lapse τ, and $\Delta V/V = -\Delta\tau/\tau$ and is constant along the whole seismogram (Poupinet et al., 1984). Because the two techniques yielded similar results (Renalier, 2010), only those of the doublet technique are presented here.

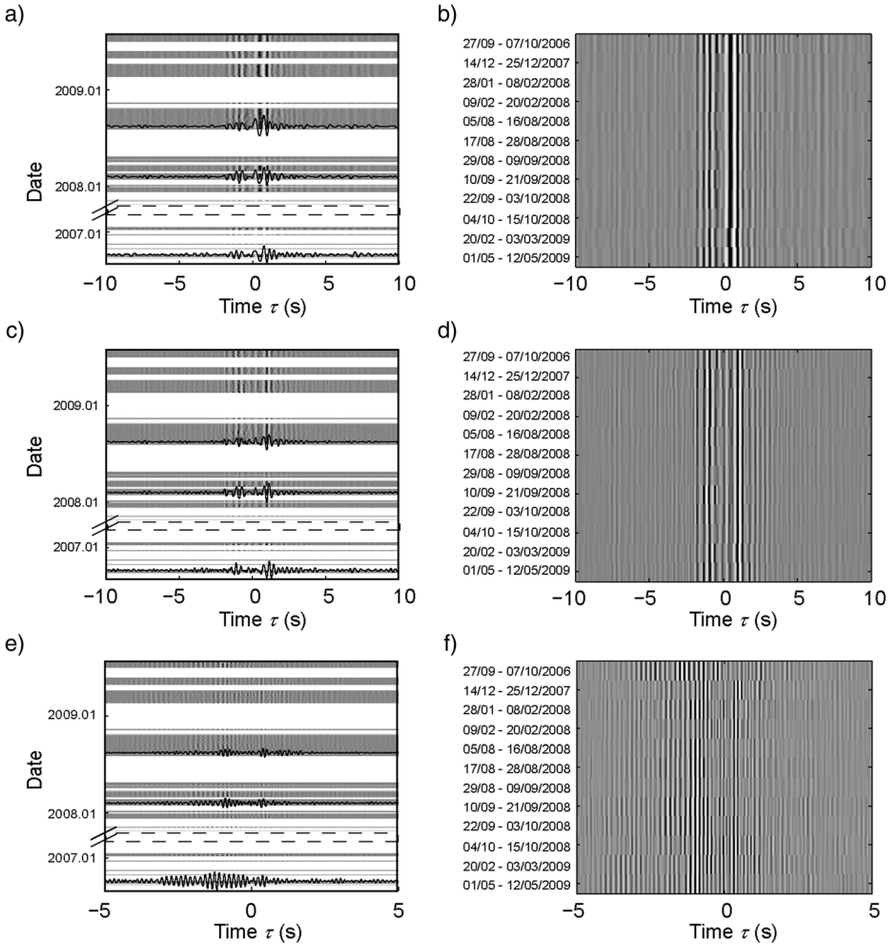

Figure 10. Crosscorrelation functions computed along time in different frequency ranges. (a) and (b) 1.3- to3.5-Hz, (c) and (d) 2- to 5-Hz, (e) and (f) 5- to 10-Hz frequency bands. Left column: Temporal evolution of the one-day crosscorrelation functions. Right column: comparison of twelve 12-day correlation functions.

The crosscorrelation function obtained for the whole year 2008 was chosen as the reference correlation, and temporal evolution was evaluated by comparing this reference with current correlation functions computed by crosscorrelating the seismic noise in five-day and 12-day moving windows along the three-year time period. For each current correlation function, we assessed the relative time perturbations $\Delta\tau/\tau$ by measuring the slope of the traveltime shifts $\Delta\tau$ as a function of time τ. Despite some little discrepancies relative to the hypothesis of homogeneous velocity variations ($\Delta\tau/\tau =$ constant), we could fit a linear trend on the curves $\Delta\tau = f(\tau)$ for time-lapse values τ between 1 and 7 s (see Poupinet et al., 1984; Brenguier et al., 2008 for details on the processing technique).

Figure 11 shows the relative arrival-time variations $\Delta\tau/\tau$ measured during 32 months between the two stations AP and AM, for five-day and 12-day windows. Results are similar for the two window lengths, and the time windows of 12 days are used in the following. Although measurements are discontinuous and are affected by short period variations (SP in Figure 11), the graphs for the three frequency bands show almost the same linear trend (highlighted with the dashed line in Figure 11), with an increase in arrival times of about 0.2% per year measured by linear regression for the 2- to 5-Hz frequency band. This variation in the correlation function could result from distance variation resulting from differential motion of the two stations, which are installed on the landslide.

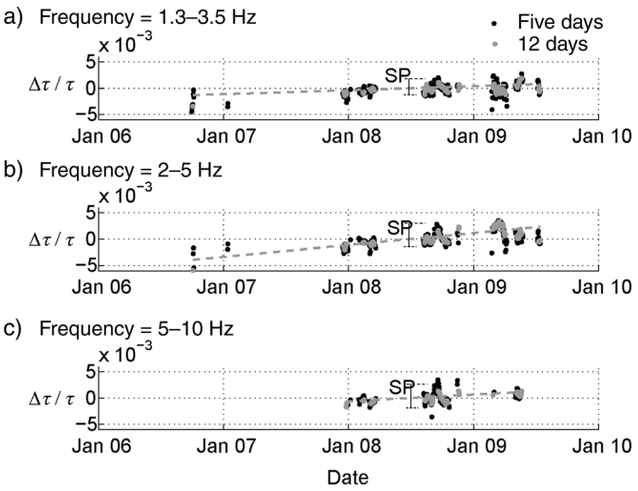

Figure 11. Evolution of relative arrival times $\Delta\tau/\tau$ between October 2006 and May 2009, measured with the doublet technique, for the three frequency bands: (a) 1.3–3.5 Hz, (b) 2–5 Hz, and (c) 5–10 Hz. When differences result only from homogeneous velocity variations, $\Delta\tau/\tau = -\Delta V/V$ (where V is the seismic velocity in the medium). SP: short-period variations; gray dashed line: long-term tendency computed by linear regression on the 12-day moving windows.

However, the biannual GPS measurements (Jongmans et al., 2009), along with two aerial Lidar campaigns in November 2006 and April 2009 (U. Kniess, personal communication, 2009), indicate that the distance of 250 m between the two stations has not varied by more than 15 cm during that period. This differential displacement corresponds to a traveltime increase of less than 0.06%, which is far lower than the 0.2% variation detected with seismic monitoring. This comparison indicates that the observed traveltime increase corresponds to a seismic ground-velocity decrease. That decrease probably is linked to the landslide continuously exerting a damaging effect, which has already reduced V_S by a factor of 2 in the shallow active zone at the toe of the landslide (Figure 3). Although these results have to be confirmed by longer and continuous data, they highlight the potential of the crosscorrelation technique for monitoring landslide activity.

Conclusions

Among the different geophysical parameters, shear-wave velocity V_S has emerged as being of major importance for characterizing landslides because of its sensitivity to compaction or to the degree of fissuring in soils and rocks. In the case of the clayey Avignonet landslide, V_S measurements have provided valuable information on the deformation state of the clay material, which resulted from the gravitational movement along slip surfaces at three different depths (at about 5 m, 15 m, and 45 m).

Both lateral and vertical variations of V_S have been related to the landslide activity and to the location of slip surfaces. Different techniques for in situ measurement of V_S have been tested. Linear arrays of geophones with active sources offer the advantage of good resolution in the surficial layers and can detect the two shallower slip surfaces (at about 5 m and 15 m) highlighted by vertical V_S contrasts. In addition, SH refraction tests provided 2D images that have relatively limited penetration (25–30 m) because of the weak energy of the source. Surface-wave inversion with an active source was limited to a few tens of meters in penetration, too, because of the low energy of the source at low frequencies and/or the high-pass frequency filtering of the geophones used (4.5 Hz).

In addition to the requirement that the local geometry be stratified horizontally, this study also pointed to the problem of secondary scattering sources (which are present in strongly perturbed zones) for linear arrays. Such scattering sources may generate higher modes and destroy the coherency of the surface-wave fundamental mode, even

for a group of geophones located over a 1D medium. A small-aperture 2D array of six short-period seismometers (maximum size of 120 m in this case), which measures ambient vibrations from all azimuths, was used successfully for surface-wave inversion in a horizontally stratified zone. This passive technique extracted lower-frequency surface waves from seismic records of one-hour duration and characterized the V_S contrast at the bottom of the landslide. However, the technique was found to be excessively time- and effort-consuming for 3D mapping of the whole landslide. To overcome that limitation, we deployed a large-aperture array of 11 stations (1- × 1-km in size) covering the southern part of the landslide where geotechnical information was available.

Seismic noise was recorded during two weeks. Combining ambient noise crosscorrelation with records of explosive shots performed close to each station, a 3D V_S image of the landslide was inverted from surface-wave group-dispersion curves. Although the lateral resolution is low (about 100 m) because of the limited number of stations, the V_S image obtained is consistent with the depth of the landslide found in boreholes. Major advantages of this method are that manpower is required only during instrument installation and withdrawal, and that secondary scattering sources — which always exist in active landslides — help to fulfill the diffuse wavefield assumption. Finally, the crosscorrelation technique was applied to the records from two permanent stations during a 30-month period. Associated with seismic monitoring techniques, the crosscorrelation technique allowed detection of a slight but significant decrease in surface-wave velocities. This result offers new perspectives for monitoring such landslides and for detecting rheological variations in clay when a slide evolves to a flow.

Acknowledgments

The authors thank C. Pequegnat and E. Bourova for preprocessing the seismological data, R. Béthoux for maintaining instrumentation, and all the people who participated in the field investigation. This study was supported in part by the European project NERIES, by the French ANR projects ECOUPREF and SISCA, by the LCPC Sécheresse program, by the Isère Department through the Pôle Grenoblois des Risques Naturels, and by the ERC Advanced Grant Whisper. The French landslide observatory OMIV (www-lgit.obs.ujf-grenoble.fr/observations/omiv) provided data from the permanent seismological stations. We thank two anonymous reviewers for their valuable comments.

REFERENCES

Aki, K., 1957, Space and time spectra of stationary stochastic waves, with special reference to microtremors: Bulletin of Earthquake Research Institute, **35**, 415–456.

Aki, K., and B. Chouet, 1975, Origin of coda waves: source, attenuation, and scattering effects: Journal of Geophysical Research — Solid Earth, **80**, 3322–3342.

Aki, K., and P. G. Richards, 1980, Quantitative seismology: Theory and methods: W. H. Freeman.

Andrus, R., P. Piratheepan, B. S. Ellis, J. Zhang, and C. H. Juang, 2004, Comparing liquefaction evaluation methods using penetration-V_S relationships: Soil Dynamics and Earthquake Engineering, **24**, 713–721.

Asten, M. W., and J. D. Henstridge, 1984, Array estimators and use of microseisms for reconnaissance of sedimentary basins: Geophysics, **49**, 1828–1837.

Bard, P.-Y., and J. Riepl-Thomas, 1999, Wave propagation in complex geological structures and local effects on strong ground motion, *in* E. Kausel and G. Manolis, eds., Wave motion in earthquake engineering: International Series Advances in Earthquake Engineering, WIT Press, 37–95.

Barmin, M. P., M. H. Ritzwoller, and A. L. Levshin, 2001, A fast and reliable method for surface wave tomography: Pure and Applied Geophysics, **158**, 1351–1375.

Bièvre, G., F. Renalier, L. Valldosera, D. Jongmans, E. Flavigny, and P. Foray, 2010, Caractéristiques de l'endommagement d'une argile par méthodes sismiques: Proceedings of the "Journéees Nationales de Géologie et Géotechnique."

Boore, D., 2006, Determining subsurface shear-wave velocities: a review: Paper presented at the Third International Symposium on the Effects of Surface Geology on Seismic Motion, paper no. 103.

Brenguier, F., N. M. Shapiro, M. Campillo, V. Ferrazzini, Z. Duputel, O. Coutant, and A. Nercessian, 2008, Towards forecasting volcanic eruptions using seismic noise: Nature Geoscience, **1**, 126–130.

Brenguier, F., N. M. Shapiro, M. Campillo, A. Nercessian, and V. Ferrazzini, 2007, 3-D surface wave tomography of the Piton de la Fournaise volcano using seismic noise correlations: Geophysical Research Letters, **34**, L02305.

Bryan, G. M., and R. D Stoll, 1988, The dynamic shear modulus of marine sediments: Journal of the Acoustical Society of America, **83**, 2159–2164.

Claerbout, J. F., 1968, Synthesis of a layered medium from its acoustic transmission response: Geophysics, **33**, 264–269.

Dal Moro, G., M. Pipan, and P. Gabrielli, 2007, Rayleigh wave dispersion curve inversion via genetic algorithms

and marginal posterior probability density estimation: Journal of Applied Geophysics, **61**, 39–55.

Dasios, A., C. McCann, T. Astin, D. McCann, and P. Fenning, 1999, Seismic imaging of the shallow subsurface: Shear wave case histories: Geophysical Prospecting, **47**, 565–591.

Dines, K., and J. Lyttle, 1979, Computerized geophysical tomography: Proceedings of the Institute of Electrical and Electronics Engineers, **67**, 106–1073.

Finn, W., 2000, State-of-the-art of geotechnical earthquake engineering practice: Soil Dynamics and Earthquake Engineering, **20**, 1–15.

Finn, W., and A. Wightman, 2003, Ground motion amplification factors for the proposed 2005 edition of the National Building Code of Canada: Canadian Journal of Civil Engineering, **30**, 272–278.

Ghose, R., and J. Goudswaard, 2004, Integrating S-wave seismic-reflection data and cone-penetration-test data using a multiangle multiscale approach: Geophysics, **69**, 440–459.

Giraud, A., P. Antoine, T. van Asch, and J. Nieyuwenhuis, 1991, Geotechnical problems caused by glaciolacustrine clays in the French Alps: Engineering Geology, **31**, 185–195.

Gouédard, P., L. Stehly, F. Brenguier, M. Campillo, Y. C. de Verdière, E. Larose, L. Margerin, P. Roux, F. J. Sánchez-Sesma, N. M. Shapiro, and R. L. Weaver, 2008, Cross-correlation of random fields: Mathematical approach and applications: Geophysical Prospecting, **56**, 375–393.

Grandjean, G., and A. Bitri, 2006, 2M-MASW: Multifold and multichannel seismic inversion of local dispersion of Rayleigh waves in laterally heterogeneous subsurfaces: Application to the Super-Sauze earthflow (France): Near Surface Geophysics, **4**, no. 6, 367–375.

Hadziioannou, C., E. Larose, O. Coutant, P. Roux, and M. Campillo, 2009, Stability of monitoring weak changes in multiply scattering media with ambient noise correlation: Laboratory experiments: Journal of the Acoustical Society of America, **125**, 3688–3695.

Hasancebi, N., and R. Ulusay, 2007, Empirical correlations between shear wave velocity and penetration resistance for ground-shaking assessments: Bulletin of Engineering Geology and the Environment, **66**, 203–213.

Hegazy, Y., and P. Mayne, 1995, Statistical correlations between V_S and cone penetration data for different soil types: International Symposium on Cone Penetration Testing, 173–178.

Herrmann, R. B., 1973, Surface wave generation by the south central Illinois earthquake of November 9, 1968: Bulletin of the Seismological Society of America, **63**, no. 6, 2121–2134.

———, 1987, Computer programs in seismology, IV: Surface wave inversion: Saint Louis University.

Hunter, J., B. Benjumea, J. Harris, R. Miller, S. Pullan, and R. A. Burns, 2002, Surface and downhole shear wave seismic methods for thick soil site investigations: Soil Dynamics and Earthquake Engineering, **22**, 931–941.

Jongmans, D., 1992, The application of seismic methods for dynamic characterization of soils in earthquake engineering: Bulletin of the International Association of Engineering Geology, **46**, 63–69.

Jongmans, D., G. Bièvre, S. Schwartz, F. Renalier, N. Beaurez, and Y. Orengo, 2009, Geophysical investigation of a large landslide in glaciolacustrine clays in the Trièves area (French Alps): Engineering Geology, **109**, 45–56.

Keilis-Borok, V. I., 1986, Seismic surface waves in a laterally inhomogeneous earth: Kluwer Academic Publishers.

Kim, D., and H. Park, 1999, Evaluation of ground densification using SASW method and resonant column tests: Canadian Geotechnical Journal, **36**, 291–299.

Lacoss, R., E. J. Kelly, and M. N. Toksöz, 1969, Estimation of seismic noise using arrays: Geophysics, **34**, 21.

Lee, J., and J. Santamarina, 2005, Bender elements: Performance and signal interpretation: Journal of Geotechnical and Geoenvironmental Engineering, **131**, 1063–1070.

Lin, C.-P., and C.-H. Lin, 2007, Effect of lateral heterogeneity on surface wave testing: Numerical simulations and a countermeasure: Soil Dynamics and Earthquake Engineering, **27**, 541–552.

Méric, O., S. Garambois, D. Jongmans, J. Vengeon, M. Wathelet, and J. Châtelain, 2005, Application of geophysical methods for the investigation of the large gravitational mass movement of Sechilienne (France): Canadian Geotechnical Journal, **42**, 1105–1115.

Miller, R., J. Xia, C. Park, and J. Ivanov, 1999, Multichannel analysis of surface waves to map bedrock: The Leading Edge, **18**, 1392–1396.

Mondol, N. H., K. Bjørlykke, J. Jahren, and K. Høeg, 2007, Experimental mechanical compaction of clay mineral aggregates — Changes in physical properties of mudstones during burial: Marine and Petroleum Geology, **24**, 289–311.

Ohrnberger, M., E. Schissele, C. Cornou, S. Bonnefoy-Claudet, M. Wathelet, A. Savvaidis, F. Scherbaum, and D. Jongmans, 2004, Frequency wavenumber and spatial autocorrelation methods for dispersion curve determination from ambient vibration recordings: Paper presented at the 13th World Conference on Earthquake Engineering.

Okada, H., 2003, The microtremor survey method (K. Suto, trans.): SEG Geophysical Monograph Series No. 12.

Nunziata, C., G. De Nisco, and G. F. Panza, 2009, S-waves profiles from noise cross correlation at small scale: Engineering Geology, **105**, 161–170.

Park, C., R. Miller, and J. Xia, 1999, Multi-channel analysis of surface waves: Geophysics, **64**, 800–808.

Park, C. B., R. D. Miller, J. Xia, and J. Ivanov, 2007, Multichannel analysis of surface waves (MASW) — Active and passive methods: The Leading Edge, **26**, no. 1, 60–64.

Parolai, S., M. Picozzi, S. M. Richwalski, and C. Milkereit, 2005, Joint inversion of phase velocity dispersion and H/V ratio curves from seismic noise recordings using a genetic algorithm, considering higher modes: Geophysical Research Letters, **32**, L01303.

Picozzi, M., S. Parolai, D. Bindi, and A. Strollo, 2009, Characterization of shallow geology by high frequency seismic noise tomography: Geophysical Journal International, **176**, 164–174.

Poupinet, G., W. L. Ellsworth, and J. Fréchet, 1984, Monitoring velocity variations in the crust using earthquake doublets: An application to the Calaveras Fault, California: Journal of Geophysical Research, **89**, 5719–5731.

Renalier, F., 2010, Caractérisation sismique de sites hétérogènes à partir de méthodes actives et passives: variations latérales et temporelles: Ph.D. thesis, Université de Grenoble, France.

Richwalski, S. M., M. Picozzi, S. Parolai, C. Milkereit, F. Baliva, D. Albarello, K. Roy-Chowdhury, H. van der Meer, and J. Zschau, 2007, Rayleigh wave dispersion curves from seismological and engineering-geotechnical methods: A comparison at the Bornheim test site (Germany): Journal of Geophysics and Engineering, **4,** no. 4, 349.

Roux, P., 2009, Passive seismic imaging with directive ambient noise: Application to surface waves and the San Andreas Fault in Parkfield, CA: Geophysical Journal International, **179**, 367–373.

Sambridge, M., 1999, Geophysical inversion with a neighbourhood algorithm, I: Searching a parameter space: Geophysical Journal International, **138**, 479–494.

Sánchez-Sesma, F. J., and M. Campillo, 2006, Retrieval of the Green function from cross correlation: the canonical elastic problem: Bulletin of the Seismological Society of America, **96**, 1182–1191.

Satoh, T., H. Kawase, and S. Matsushima, 2001, Estimation of S-wave velocity structures in and around the Sendai Basin, Japan, using array records of microtremors: Bulletin of the Seismological Society of America, **91**, 206–218.

Scherbaum, F., K.-G. Hinzen, and M. Ohrnberger, 2003, Determination of shallow shear wave velocity profiles in the Cologne/Germany area using ambient vibrations: Geophysical Journal International, **152**, 597–612.

Schlue, J. W., and K. K. Hostettler, 1987, Rayleigh wave phase velocities and amplitude values in the presence of lateral heterogeneities: Bulletin of the Seismological Society of America, **77**, 244–255.

Schuster, G. T., J. Yu, J. Sheng, and J. Rickett, 2004, Interferometric/daylight seismic imaging: Geophysical Journal International, **157**, 838–852.

Sens-Schönfelder, C., and U. Wegler, 2006, Passive image interferometry and seasonal variations of seismic velocities at Merapi Volcano, Indonesia: Geophysical Research Letters, **33**, L21302.

Shapiro, N., and M. Campillo, 2004, Emergence of broadband Rayleigh waves from correlations of the ambient seismic noise: Geophysical Research Letters, **31**, L07614.

Socco, L., and D. Jongmans, 2004, Special issue on seismic surface waves: Near Surface Geophysics, **2**, 163–165.

Socco, L. V., and C. Strobbia, 2004, Surface-wave method for near-surface characterization: A tutorial: Near Surface Geophysics, **2**, 165–185.

Socco, L., D. Boiero, C. Comina, S. Foti, and R. Wìsén, 2008, Seismic characterization of an Alpine site: Near Surface Geophysics, **6**, 255–267.

Socco, L. V., D. Boiero, S. Foti, and R. Wisén, 2009, Laterally constrained inversion of ground roll from seismic reflection records: Geophysics, **74**, no. 6, G35–G45.

Sommerville, P., and R. Graves, 2003, Characterization of earthquake strong ground motion: Pure and Applied Geophysics, **160**, 1811.

Stehly, L., M. Campillo, and N. M. Shapiro, 2006, A study of the seismic noise from its long range correlation properties: Journal of Geophysical Research, **111**, B10306.

Stockwell, R. G., L. Mansinha, and R. P. Lowe, 1996, Localization of the complex spectrum: the S transform: IEEE transactions on signal processing, **44**, 998–1001.

Tokimatsu, K., 1997, Geotechnical site characterization using surface waves: First International Conference on Earthquake and Geotechnical Engineering, 1333–1368.

Tokimatsu, K., S. Tamura, and H. Kojima, 1992, Effects of multiple modes on Rayleigh wave dispersion characteristics: Journal of Geotechnical Engineering, **118**, 1529–1543.

Uebayashi, H., 2003, Extrapolation of irregular subsurface structures using the horizontal-to-vertical ratio long-period microtremors: Bulletin of the Seismological Society of America, **93**, 570–582.

Wapenaar, K., D. Draganov, and J. O. A. Robertson, 2008, Seismic interferometry: History and present status: SEG Geophysics Reprint Series No. 26.

Wathelet, M., 2008, An improved neighborhood algorithm: parameter conditions and dynamic scaling: Geophysical Research Letters, **35**, L09301.

Wathelet, M., D. Jongmans, and M. Ohrnberger, 2004, Surface wave inversion using a direct search algorithm and its application to ambient vibration measurements: Near Surface Geophysics, **2**, 211–221.

Wathelet, M., D. Jongmans, M. Ohrnberger, and S. Bonnefoy-Claudet, 2008, Array performances for ambient vibrations on a shallow structure and consequences over V_S inversion: Journal of Seismology, **12**, 1–19.